Engineering Structures 152 (2017) 790–803

Contents lists available at ScienceDirect

Engineering Structures

journal homepage: www.elsevier.com/locate/engstruct

Non linear vertical-rocking isolation system: Application to legged wine storage tanks

Gaspar A. Auad *, José L. Almazán

Department of Structural Engineering, Pontificia Universidad Católica de Chile, Casilla 306, Correo 22, Santiago, Chile

ARTICLE INFO

Article history:
Received 21 June 2017
Revised 25 September 2017
Accepted 29 September 2017

Keywords:
Three-dimensional seismic isolation
Non-lineal seismic isolation
Fluid-structure interaction
Stainless steel tanks
Legged wine storage tanks
Finite element method
Fragility analysis

ABSTRACT

In the last 30 years, there has been a great development of seismic isolation systems. The most used are elastomeric type devices and frictional pendulum bearings. Although different, both types generate horizontal seismic isolation, but not vertical. This study presents a nonlinear three-dimensional seismic isolation system called vertical rocking isolation (VRI) system, based on devices called ISO3D. Unlike conventional seismic isolators, the ISO3D device is vertically flexible and laterally stiff. Although the proposed system can be applied to any type of structure, it is particularly attractive as a seismic protection system of special structures, such as fluid storage tanks supported on legs, power transformers and sensitive equipment with vertical acceleration. In this research an application to legged wine storage tanks is presented. Two models were studied: a 3 m^3 tank with 4 legs, and a 30 m^3 tank with 6 legs. The fluid-structure interaction was considered using a quasi-static approach, where the fluid behaves as a mass attached to the tank walls. Time-history analyses results show average reductions of axial loads and shear loads on the legs of 57% and 61%, respectively. Finally, a fragility analysis indicates that the PGA required to reach 50% of probability of failure increases by an average of 153% by using the VRI system.

1. Introduction

During last 30 years there has been a great development of seismic isolation systems. The most used are elastomeric type devices, with and without a lead core, and frictional pendulum bearings, with single and double curvature. Although different, both devices generate horizontal seismic isolation, i.e. three lateral-torsional low frequency modes, but not vertical.

A three-dimensional seismic isolation system called GERB-BCS (Base Control System), which consists of a set of helical compression springs and viscous dampers on which the structure rests is available. With the use of these devices, the structure can be seismically isolated both horizontally and vertically. The principle of operation is identical to the well-known concept of vibration isolation in industrial equipment, i.e. six low frequency modes: three lateral-torsional modes, and three vertical-rocking modes.

The aforementioned systems can be used for any type of structure (buildings, industrial facilities, or equipment). Several authors have proposed seismic isolation systems designed for specific applications. For example, for fluid storage, the following can be mentioned: Shrimali and Jangrid [1], Cho et al. [2], Panchal and Jangid [3,4], Abali and Uckan [5], Shekari et al. [6]; and Soni et al. [7]. In order to seismically protect light structures such as legged wine storage tanks, the Rubber-Layer Rolling Bearing (RLRB) device [8,9] can be used. This kind of base isolation device, apart from reducing the lateral seismic loads, could reduce the axial loads and avoid leg buckling. Another way to seismically protect structures is through the use of energy dissipators. A novel system of dissipation that allows to reduce the vertical loads is described by Foti et al. [10].

The seismic behavior of storage structures has been studied extensively. For silos containing grain-like material, the following studies can be mentioned: Silvetry et al. [11,12]. For fluid storage, stainless steel tanks (SST) are commonly used. This type of structure is probably one of the most vulnerable to earthquake damage. The use of SST for fermentation and wine storage began in the 1950s in USA [13], and approximately three decades later in Chile and Argentina. The main advantages of SST over tanks made of other materials are: (i) ease of cleaning; (ii) relative chemical inertness; (iii) improved control of the fermentation process; and (iv) their aesthetic appeal. Thus, reinforced concrete tanks have been replaced almost completely by SST. Nevertheless, the first generation of SST was not designed considering earthquake resistant criteria. The ease of construction and use of a minimal amount of material were probably the prevailing criteria in early designs

* Corresponding author.
E-mail address: gaauad@uc.cl (G.A. Auad).

https://doi.org/10.1016/j.engstruct.2017.09.061
0141-0296/

Nomenclature

α	angle of inclination of damper wedge
β	isolator slenderness as a function of vertical deformation, $b(u)/H_o$
β_o	isolator initial slenderness, b_o/H_o
$\ddot{d}_{gx}$	ground acceleration in the X-direction
$\ddot{d}_{gy}$	ground acceleration in the Y-direction
Γ_1	surface with null relative pressure
Γ_2	contact surface between fluid and structure
$\hat{\omega}$	frequency of the vertical deformation to calculate equivalent stiffness
$\hat{f}_o$	dimensionless expression for f_o
$\hat{f}_u$	dimensionless expression for f_u
$\hat{k}_u$	dimensionless expression for k_u
$\hat{u}$	dimensionless expression for $u, u/H_o$
PGA_h	horizontal peak ground acceleration
μ	steel on steel friction coefficient
Ω	volumetric domain
ω_z	vertical low frequency
$\omega_{\theta x}$	rocking around the X-axis low frequency
$\omega_{\theta y}$	rocking around the Y-axis low frequency
Ω_x	dimensionless relationship between vertical stiffness and mass distribution, ρ_{sx}/ρ_{mx}
Ω_y	dimensionless relationship between vertical stiffness and mass distribution, ρ_{sy}/ρ_{my}
ϕ	steel on steel friction angle
ρ	wine density
ρ_{mx}	mass radii of gyration with respect to the X-axis
ρ_{my}	mass radii of gyration with respect to the Y-axis
ρ_{sx}	stiffness radii of gyration with respect to the X-axis
ρ_{sy}	stiffness radii of gyration with respect to the Y-axis
$\ddot{\boldsymbol{d}}_g$	ground acceleration vector
$\ddot{\boldsymbol{q}}_a$	absolute fluid acceleration
$\hat{\boldsymbol{n}}$	vector in normal direction to tank surface
$\boldsymbol{C}$	structure viscous damping matrix
$\boldsymbol{F_u}$	vector of non-linear vertical forces
$\boldsymbol{K}$	structure stiffness matrix
$\boldsymbol{L_f}$	kinematic transformation matrix of non-linear vertical forces
$\boldsymbol{M_f}$	attached fluid mass matrix
$\boldsymbol{M}$	structure mass matrix
$\boldsymbol{N_p}$	matrix of the shape functions corresponding to the hydrodynamic pressure
$\boldsymbol{N_q}$	matrix of the shape functions corresponding to the displacement field of the structure
$\boldsymbol{P}(t)$	nodal hydrodynamic pressure
$\boldsymbol{q}(t)$	nodal displacement of the structure
$\boldsymbol{R}$	structure incidence matrix
$\boldsymbol{S}$	fluid-structure interaction matrix
ξ	damping ratio
$b(u)$	isolator opening as a function of vertical deformation
b_o	isolator initial opening
b_p	damper plates width
C	spring index, D/d
c	velocity of the compression wave in wine
D	spring mean diameter
d	spring wire diameter
E	elastic modulus of the steel
e_p	damper plates thickness
f	isolator non linear vertical force
f_o	spring pre-stressing load
f_s	spring load
f_u	isolator vertical elastic force
f_μ	damper vertical force
H_o	isolator initial height
h_p	damper plates height
I	damper plates flexural moment of inertia
K_b	modulus of volumetric compressibility
k_p	lateral stiffness of dampers plates
k_s	spring stiffness
k_u	isolator vertical elastic stiffness
K_z	total equivalent vertical stiffness
k_{zj}	equivalent vertical stiffness of the j-th isolator
L	isolator axis distance
M	moment in torsion spring
m	mass of the structure, assuming rigid body
N	leg axial force
N_a	spring active coils or wave
P	force in extension or compression spring
p	hydrodynamic pressure
q	displacement of the structure
S	spring stress
s	spring deformation
t	wall tank thickness
u	isolator vertical deformation
$U(\cdot)$	heaviside function
u_h	half amplitude of the vertical deformation to calculate equivalent stiffness
u_o	damper gap length
V	leg total shear force
v	damper plates lateral deformation
V_r	leg radial shear force
V_t	leg tangential shear force

[13]. Consequently, destructive earthquakes put these early designs of SST to test, often with poor results. The seismic performance of wine tanks has been recorded several times: Caucete Earthquake [14,15], Greenville [16], Morgan Hill [17], Loma Prieta [18], San Simeon [19], and Lake Grassmere [20]. But the event that has certainly brought greater information has been the Maule Earthquake [21,22]. This earthquake affected almost all Chilean wineries. Losses amounted to approximately 125 million liters of wine, representing 12.5% of production in 2009. The earthquake struck a week before the beginning of the harvest, when only 50% of storage tanks were in use. This indicates that more than 25% of tanks with wine lost all or part of their content. Wine tanks can be classified in two groups: (a) flat base (or continuous support) tanks; and, (b) legged tanks. The first are used to store volumes between 30 m^3 and 400 m^3; while the latter are used for volumes between 2 m^3 and 50 m^3. Smaller, legged tanks store the best-quality wine, however, so their potential failure can cause major economic losses. The main components of the legged tanks, and typical failures observed during the Maule Earthquake are shown in Fig. 1.

This research presents a nonlinear three-dimensional seismic isolation system called vertical rocking isolation (VRI) system, which is based on devices called ISO3D. Unlike conventional seismic isolators, the ISO3D device is vertically flexible and laterally stiff. The seminal idea was proposed by Almazán et al. [23], where linear behavior of the devices was considered. Although this idea can be applied to any type of structure or industrial equipment [24], the results shown here are only for legged wine storage tanks. The critical element of this type of structure are the legs, because they are very sensitive to axial load increments. One way to control the increase of compression loads on the legs is by using the VRI system. In addition, high vertical accelerations, caused by large

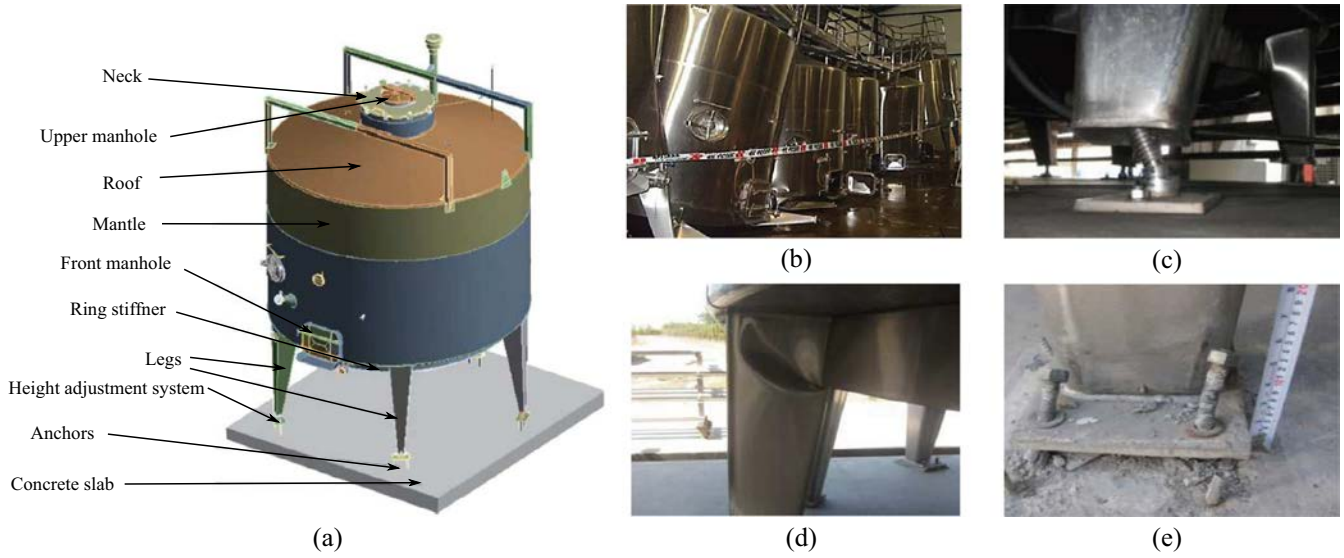

Fig. 1. (a) Scheme of a typical tank; (b) chain collapse caused by buckling in the top of leg; (c) failures of the height-adjustment devices; (d) buckling in the top of leg; (e) failure of the anchorage system.

earthquakes, raise the pressure in the contained fluid, increasing the chance of damage to the tank's mantle or loss of content.

This work has been divided into 6 parts: (i) Section 2: Description and analysis of the ISO3D devices; (ii) Section 3: Design of the VRI system; (iii) Section 4: Fluid-structure interaction model; (iv) Section 5: Case Studies; (v) Section 6: Fragility analysis; and (vi) Section 7: Conclusions.

2. Description and analysis of the isolation devices

The device that forms the proposed 3D isolation system consists of three parts: (1) an articulated frame, (2) a system of springs, and (3) an energy dissipation system. The frame consists of a set of six articulated plates, which form a hexagonal prism. The springs can be classified as primary or secondary. Primary springs provide the flexibility to isolate vibrations. Secondary springs are responsible for limiting deformations caused by the structure's own weight; otherwise, the vertical deformations imposed by seismic loads would make vertical isolation through linear devices impracticable. The energy dissipation system may be composed of one or more devices, which can deform axially or rotationally.

A schematic 2D view of the frame in undeformed and deformed configurations is presented in Fig. 2(a) and (b). Two possible realizations of the device are shown in Fig. 2(c) and (d). The first one, which has been called ISO3D-A [21,25], is formed by at least one vertical compression spring and at least two horizontal tension springs, acting as primary and secondary springs, respectively. The second one, which has been called ISO3D-B, is formed by at least two torsional springs, located on each central axis of rotation of the plates, which act both as primary and secondary springs. As shown in Fig. 2, the device is flexible vertically (U-direction) and transversally (T-direction), yet longitudinally (L-direction) stiff. As mentioned, the devices should be placed in such a way that the supported structure has three flexible modes of vibration: one vertical mode, and two rocking modes.

2.1. Non-linear elastic constitutive relations

In this Subsection the generic constitutive relation of the isolation devices in the vertical direction is developed, considering only the contribution of the springs. This relation is based on two assumptions: (i) the plates behave as rigid bodies; and (ii) the springs remains in elastic range. Applying the virtual work principle, the elastic vertical force f_u provided by any spring, and its corresponding tangent stiffness k_u may be expressed as:

$$f_u = f_s \frac{\partial s}{\partial u} = (k_s s + f_o)\frac{\partial s}{\partial u} \tag{1}$$

$$k_u = \frac{\partial f_u}{\partial u} = k_s \left(\frac{\partial s}{\partial u}\right)^2 + (k_s s + f_o)\frac{\partial^2 s}{\partial u^2} \tag{2}$$

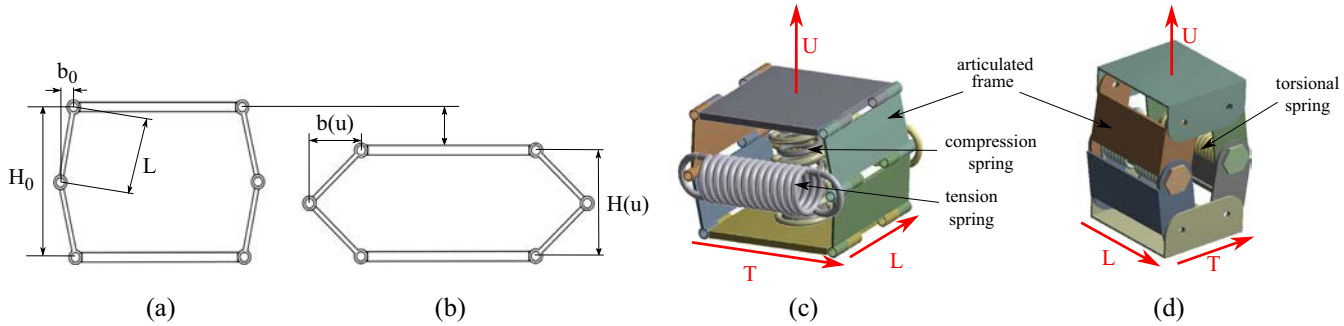

Fig. 2. (a) Frame in undeformed configuration; (b) frame in deformed configuration; (c) ISO3D-A device; (d) ISO3D-B device.

where u is the vertical deformation of the device; s and k_s are, respectively, the deformation and stiffness of the spring; $f_s = k_s s + f_o$ is the load in the spring; and f_o is the pre-stressing load (if any). To facilitate the physical interpretation and design of the devices, dimensionless expressions for f_u and k_u, for linear and torsion springs, have been obtained. These expressions are presented in Table 1. Furthermore, the expressions for the stiffness and stresses in the springs obtained by the classic spring theory [26] are shown in Table 1.

The curves for dimensionless force and dimensionless stiffness obtained for tension springs are presented in Fig. 3. A high initial stiffness is observed, because of the prevailing first term of Eq. (2), which is always positive. As the deformation increases, the stiffness decreases, becoming negative to large deformation, due to the prevailing second term of Eq. (2), which is always negative. This effect is more important when initial slenderness $\beta_o = b_o/H_o$ tends to zero and pre-stressing load f_o increases.

The curves for dimensionless force and dimensionless stiffness obtained for torsional springs are shown in Fig. 4. As with the previous case, stiffness decreases when deformation increases. Unlike the previous case, stiffness is always positive. Note that, in both cases, stiffness tends to remain constant for large deformation.

Table 1
Summary of non-linear elastic constitutive relations.

Linear spring	Torsion spring (at central axis)
$s(u) = 2(\beta - \beta_o)H_o$	$s(u) = 2(\theta - \theta_o)$
$\beta = \left(\beta_o^2 - \frac{\hat{u}}{2} - \frac{\hat{u}^2}{4}\right)^{1/2}$	$\theta = \sin^{-1}\left(\frac{1+\hat{u}}{(1+4\beta_o^2)^{1/2}}\right)$
$\frac{\partial s}{\partial u} = -\frac{1+\hat{u}}{2\beta} < 0$	$\frac{\partial s}{\partial u} = \frac{1}{H_o\left(\frac{1}{4}+\beta_o^2\right)^{1/2}\cos(\theta)} > 0$
$\frac{\partial^2 s}{\partial u^2} = -\frac{1}{H_o}\left(\frac{1}{2\beta} + \frac{(1+\hat{u})^2}{8\beta^3}\right) < 0$	$\frac{\partial^2 s}{\partial u^2} = \frac{\sin(\theta)}{2H_o^2\left(\frac{1}{4}+\beta_o^2\right)\cos^3(\theta)} > 0$
$\hat{f}_u = \frac{f_u}{k_s H_o}$; $\hat{f}_o = \frac{f_o}{k_s H_o}$	$\hat{f}_u = \frac{f_u H_o}{k_s}$
$\hat{f}_u = -\left(1 - \frac{\beta_o}{\beta} + \frac{\hat{f}_o}{2\beta}\right)(1+\hat{u})$	$\hat{f}_u = \frac{2(\theta-\theta_o)}{\left(\frac{1}{4}+\beta_o^2\right)^{1/2}\cos^3\theta}$
$\hat{k}_u = \frac{k_u}{k_s} = -\left(1 - \frac{\beta_o}{\beta} + \frac{\hat{f}_o}{2\beta}\right) - \left(2\beta - 2\beta_0 + \hat{f}_0\right)\frac{(1+\hat{u})^2}{8\beta^3} + \frac{(1+\hat{u})^2}{4\beta_o^2}$	$\hat{k}_u = \frac{k_u H_o^2}{k_s} = 8\frac{\cos(\theta)+(\theta-\theta_o)\sin(\theta)}{(1+4\beta_o^2)\cos^3(\theta)}$
$k_s = \frac{Gd^4}{8D^3 N_a}$	$k_s = \frac{Ed^4}{64DN_a}$
$S = \left(\frac{4C-1}{4C-4} + \frac{0.615}{C}\right)\frac{8PC}{\pi d^2}$	$S = \left(\frac{4C-1}{4C-4}\right)\frac{32M}{\pi d^3}$

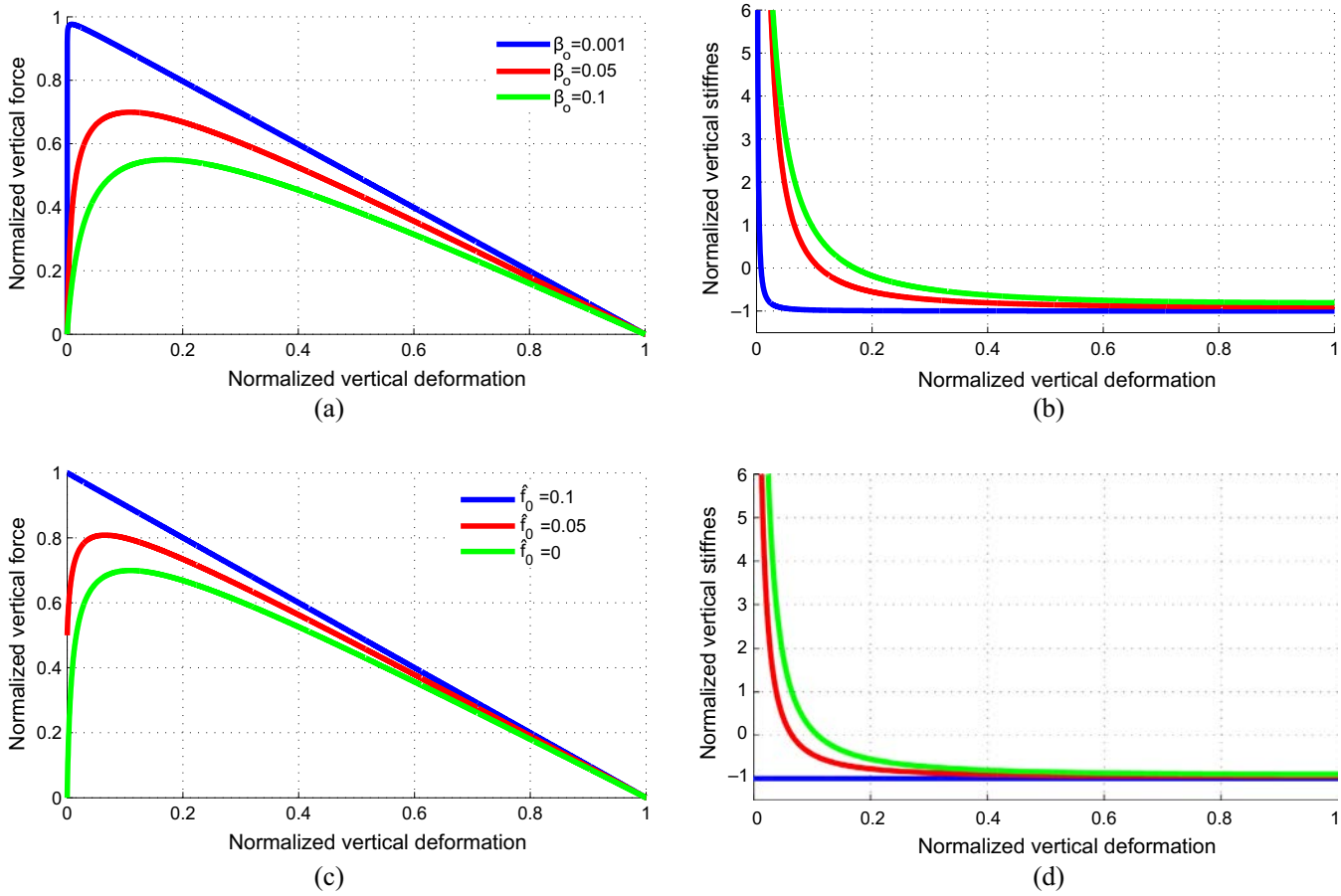

Fig. 3. Dimensionless constitutive relations for horizontal springs: (a) normalized vertical force for $\hat{f}_0 = 0$; (b) normalized vertical stiffness for $\hat{f}_0 = 0$; (c) normalized vertical force for $\beta_0 = 0.05$; (d) normalized vertical stiffness for $\beta_0 = 0.05$.

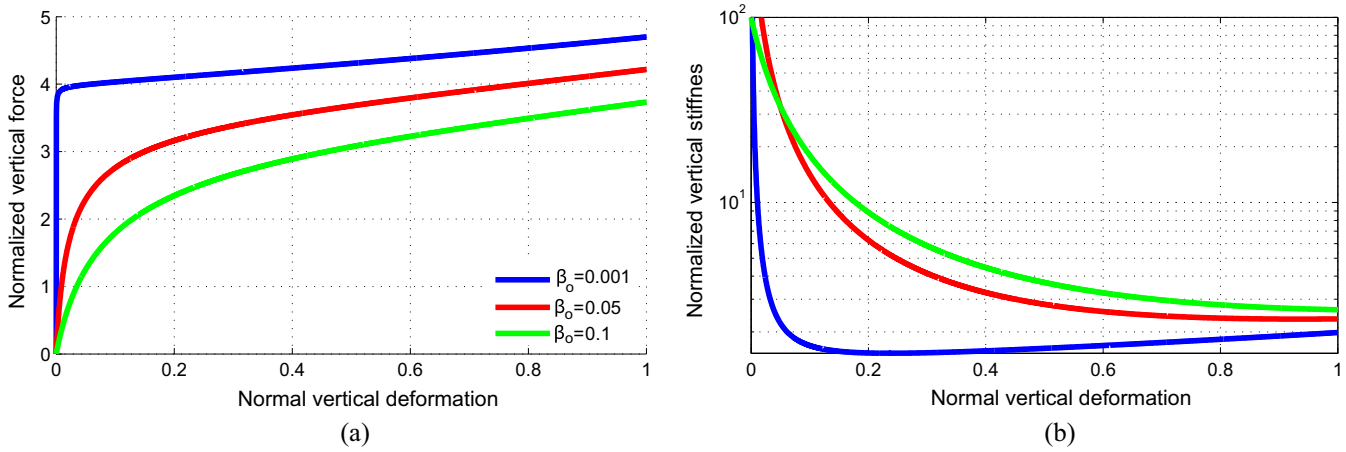

Fig. 4. Dimensionless constitutive relations for torsional springs: (a) normalized vertical force for $f_o = 0$; (b) normalized vertical stiffness for $f_o = 0$.

The vertical elastic constitutive relation of the ISO3D-A device, considering the contribution of the compression and tension springs, is very similar to that of the ISO3D-B device. Both devices present a high initial stiffness. If the isolation system is well designed, the deformation caused by the structure's own weight should be small. The initial stiffness contrasts with the low stiffness that the system possesses when seismic loads are applied, making the system suitable for vibration control.

2.2. Energy dissipation

By design, the proposed device can incorporate vertical o rotational dampers. As an example, the analysis and design of a vertical frictional damper is presented. As shown in Fig. 5(a), the damper is formed by: (i) a sliding wedge; (ii) two steel plates of thickness e_p, width b_p, and height h_p; and (iii) two brake pads attached to the upper end of the steel plates. Because of its shape, the vertical displacement u of the wedge produces a lateral deformation of the plates $v = u\tan(\alpha)$, where α is the angle of inclination of the wedge, thus creating a friction vertical force f_μ, which can be calculated as:

$$f_\mu = -2k_p \tan(\phi + \alpha \text{sign}(\dot{u}))\tan(\alpha)(u - u_o)\text{sign}(\dot{u})U(u - u_o) \qquad (3)$$

where $U(\cdot)$ is the Heaviside function; $\phi = \arctan(\mu)$ is the friction angle, μ is the friction coefficient; u_o is the length of the gap; $k_p = 3EI/h_p^3$ is the lateral stiffness of the plates, E is the elastic modulus of the steel, and $I = b_p e_p^3/12$ is the flexural moment of inertia of the plate section.

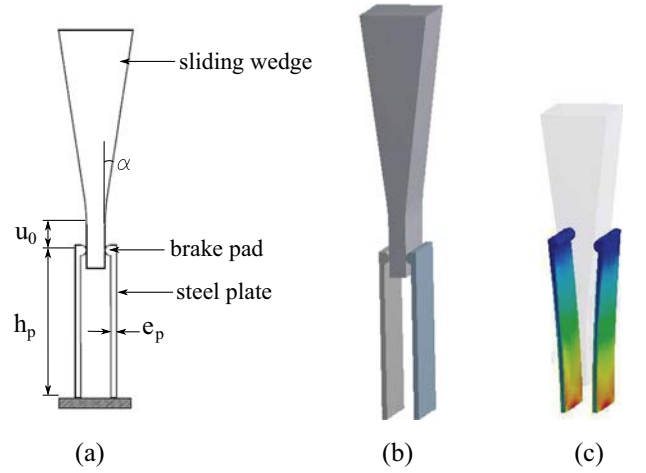

Fig. 5. Frictional damper: (a) design parameters; (b) initial configuration; (c) deformed configuration.

2.3. Equations validation

To validate the expressions presented in Table 1 and Eq. (3), finite element models (FEMs) of two devices using Ansys software [27] were performed. The plates and the springs were modeled with solid elements. The friction force in the damper was considered, however this was ignored in the joints. Equilibrium in the deformed position was considered to obtain the effects of geometric nonlinearity (material nonlinearity was not considered).

The frame geometry parameters and the properties of the springs are shown in Table 2. The ISO3D-A device is formed by two compression springs and two tension springs. The ISO3D-B device is formed by four torsion springs, two on each central axis. The design parameters of the dampers incorporated in each isolator are presented in Table 3.

A comparison of the results obtained for the ISO3D-A device is presented in Fig. 6. Both models provide very similar results. Note that for a maximum displacement of 8 cm, when the wedge contacts the lower plate of the device, the shear stress in the springs do not exceed the allowable value of 10 tonf/cm^2 (981 MPa).

The results obtained for the ISO3D-B device are shown in Fig. 7. Again, both models provide very similar results. Note that when the maximum displacement reaches 7 cm, normal stress in the

Table 2
Devices geometric properties and springs parameters.

Device	L (cm)	b_0 (cm)	spring type	# springs	d (cm)	D (cm)	N_a
ISO3D-A	18	1	compression	1	2.0	10.0	6.0
			compression	1	2.2	14.3	6.5
			horizontal	2	2.0	12.0	9.5
ISO3D-B	15	2	bending	4	1.5	9.0	6.0

Table 3
Isolators properties and dampers parameters.

Device	e_p (cm)	b_p (cm)	h_p (cm)	u_0 (cm)	α (deg)	μ
ISO3D-A	0.7	5.0	10.0	2.0	5.75	0.2
ISO3D-B	2	4.0	11.0	3.0	5.17	0.2

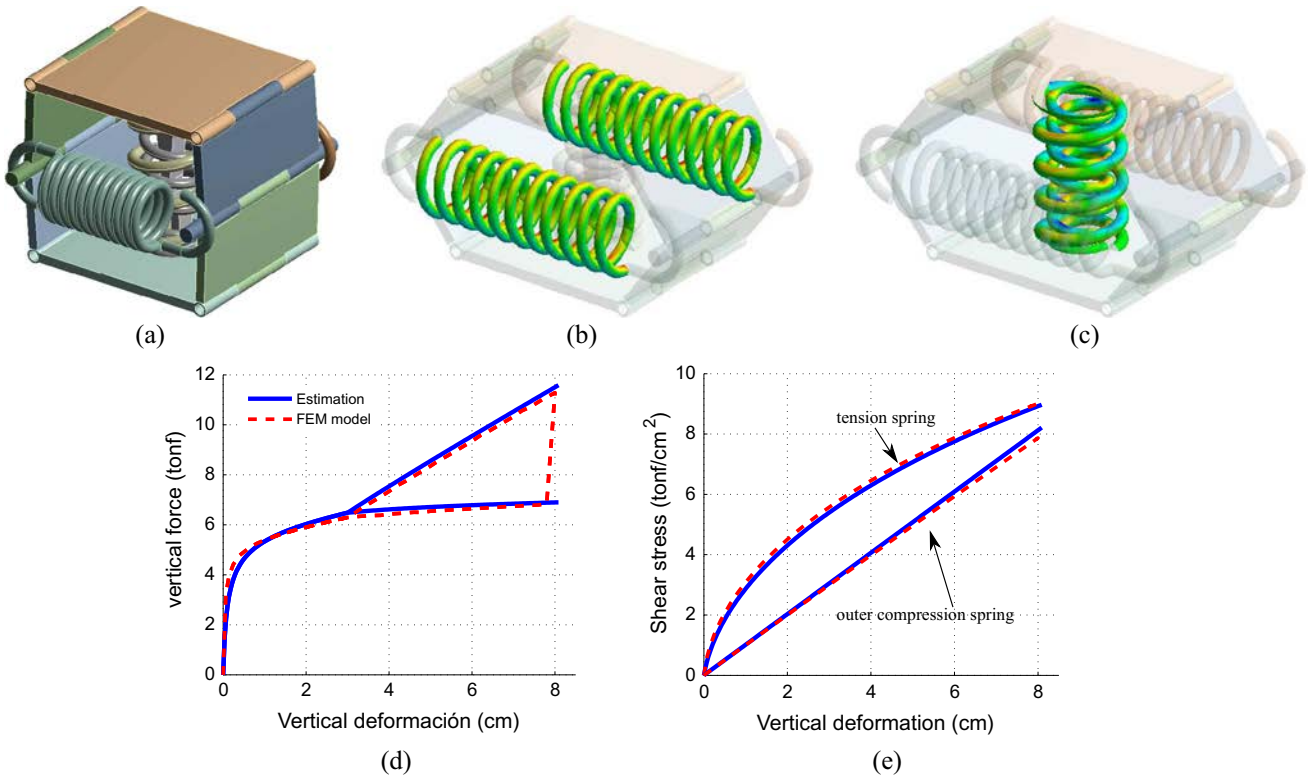

Fig. 6. ISO3D-A verification: (a) undeformed configuration; (b) deformed configuration, stress in tension springs; (c) deformed configuration, stress in compression springs; (d) isolator vertical force as a function of vertical deformation; (e) stress in springs as a function of vertical deformation.

springs do not exceed the allowable value of 14 tonf/cm^2 (1373 MPa).

Two prototypes were subjected to a cyclic test with quasi-static controlled vertical displacement. The results are shown in Appendix A.

3. Design of the vertical-rocking isolation system

As discussed in Section 2, the proposed device is flexible in the U-direction and in the T-direction, but stiff in the L-direction. One possible configuration for a structure with circular plan is presented in Fig. 8. In the case of a wine storage tank, the devices are located on the perimeter of the plan, with its stiff axis in the tangential direction. Thus, the system will have three stiff vibration modes: translation in the X-direction, translation in the Y-direction and rotation around the Z-axis; and three flexible vibration modes: translation in the Z-direction, rotation around the X-axis and rotation around the Y-axis.

Assuming that the structure is perfectly rigid with mass m, and supported on linear devices, the nominal frequencies associated with the flexible modes can be calculated as:

$$\omega_z^2 = \frac{K_z}{m} = \frac{\sum_j k_{zj}}{m} \tag{4}$$

$$\omega_{\theta x}^2 = \frac{K_z \rho_{sx}^2}{m \rho_{mx}^2} = \omega_z^2 \Omega_x^2 \tag{5}$$

$$\omega_{\theta y}^2 = \frac{K_z \rho_{sy}^2}{m \rho_{my}^2} = \omega_z^2 \Omega_y^2 \tag{6}$$

where $K_z = \sum_j k_{zj}$ is the total equivalent vertical stiffness, k_{zj} is the equivalent vertical stiffness of the j-th isolator; ρ_{mx} and ρ_{my} are the mass radii of gyration with respect to the X-axis and the Y-axis, respectively; ρ_{sx} and ρ_{sy} are the stiffness radii of gyration with respect to the X-axis and the Y-axis, respectively; $\Omega_x = \rho_{sx}/\rho_{mx} = \omega_{\theta x}/\omega_z$ and $\Omega_y = \rho_{sy}/\rho_{my} = \omega_{\theta y}/\omega_z$ are dimensionless ratios that depend on the distribution of mass and vertical stiffness.

To obtain the physical properties of the devices, it is necessary to relate the equivalent stiffness k_{zj} with the non-linear constitutive relation of the device. A simple way to relate them is using the well-known concept of harmonic equivalent stiffness, i.e.:

$$k_{zj} = \frac{\int_o^{2\pi/\hat{\omega}} f(u)u(t)dt}{\int_o^{2\pi/\hat{\omega}} u^2(t)dt} \tag{7}$$

where $f(u)$ is the non-linear constitutive relation of the device, considering both, the elastic and hysteretic components; $u(t) = u_h(1 + \sin(\hat{\omega}t))$ is the harmonic vertical deformation, $u_h = \max(u)/2$ and $\hat{\omega}$ are the half amplitude and frequency, respectively. In this case the result is independent of $\hat{\omega}$.

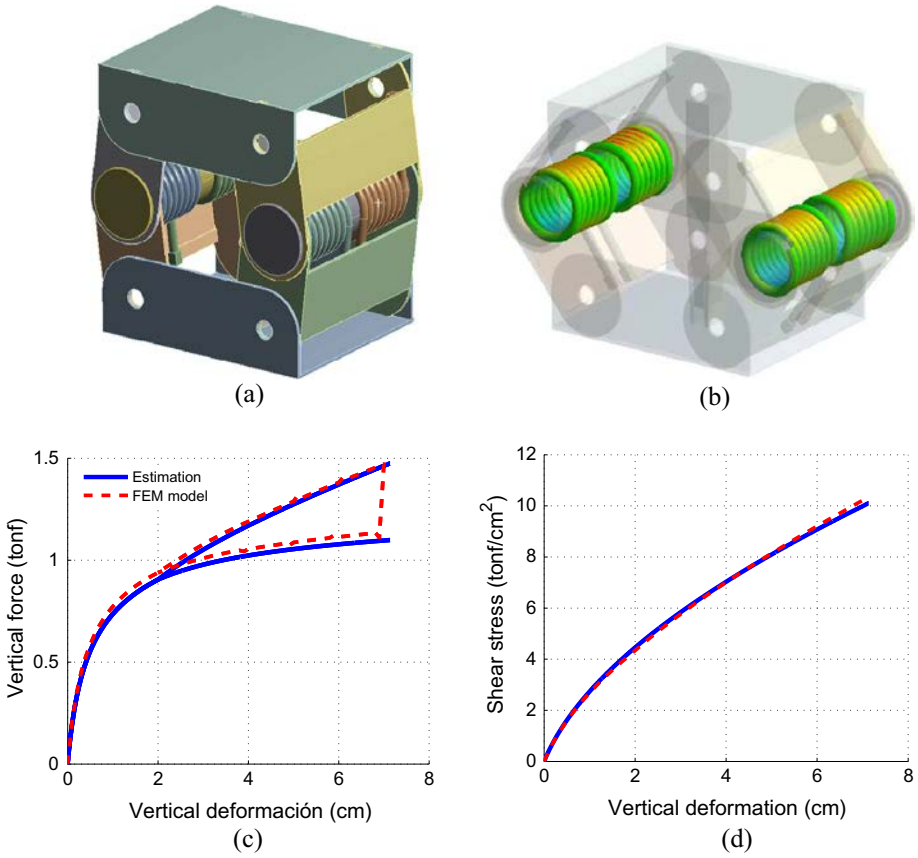

Fig. 7. ISO3D-B verification: (a) undeformed configuration; (b) deformed configuration, stress in torsional springs; (c) isolator vertical force as a function of vertical deformation; (d) stress in springs as a function of vertical deformation.

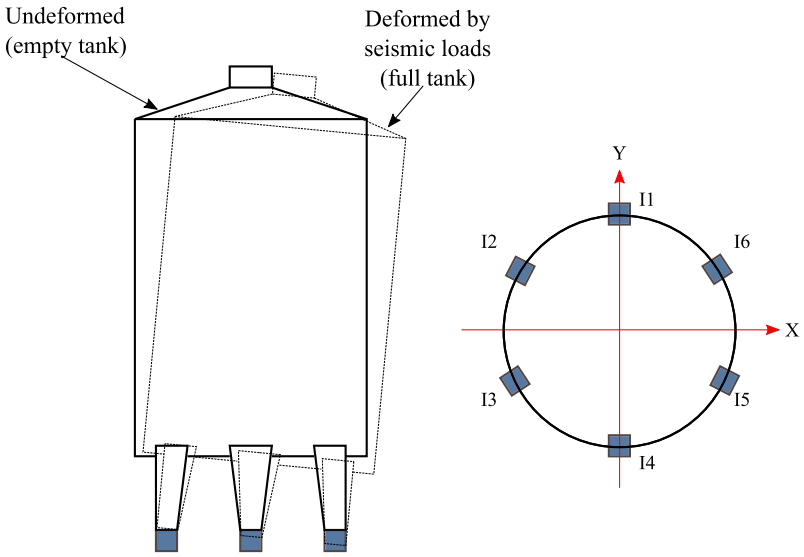

Fig. 8. Configuration of isolators under a legged wine storage tank.

4. Fluid-structure interaction model

To preserve wine quality, the tanks used for storage are always fully filled. Only a small volume of inert gas at low pressure, slightly higher than atmospheric pressure, is introduced into the tank neck. Therefore, it is reasonable to model the wine inside the tank as a non-viscous and slightly compressible fluid, with its free surface at atmospheric pressure. Thus, the differential equation in partial derivatives (Helmholtz equation) and corresponding boundary conditions are:

$$\begin{cases} \nabla^2 p - \frac{1}{c^2}\frac{\partial^2 p}{\partial t^2} = 0 & \text{in } \Omega \\ p = 0 & \text{in } \Gamma_1 \\ \frac{\partial p}{\partial \mathbf{n}} = -\rho \hat{\mathbf{n}}^T \ddot{\mathbf{q}}_a & \text{in } \Gamma_2 \end{cases} \tag{8}$$

where $p(\boldsymbol{x},t)$ is the hydrodynamic pressure; $c=\sqrt{K_b/\rho}$ is the propagation velocity of the compression wave, K_b and ρ are the modulus of volumetric compressibility and the density of the wine, respectively; Ω is the volumetric domain of the wine; Γ_1 is the free surface with null relative pressure; Γ_2 is the contact surface with the tank (wet surface), where the condition of continuity of the absolute fluid acceleration $\ddot{\boldsymbol{q}}_a$ in the normal direction $\hat{\boldsymbol{n}}$ is imposed. Applying the finite element method to the Eq. (8) the following linear ordinary differential equation is obtained [28]:

$$\boldsymbol{M_p}\ddot{\boldsymbol{P}}(t)+\boldsymbol{K}_p\boldsymbol{P}(t)=-\rho\boldsymbol{S}\ddot{\boldsymbol{q}}_a(t) \tag{9}$$

$$\boldsymbol{M_p}=\int \boldsymbol{N}_p^T\frac{1}{c^2}\boldsymbol{N}_p d\Omega \tag{10}$$

$$\boldsymbol{K_p}=\int \nabla\boldsymbol{N}_p^T\nabla\boldsymbol{N}_p d\Omega \tag{11}$$

$$\boldsymbol{S}=\int \boldsymbol{N}_p^T\hat{\boldsymbol{n}}^T\boldsymbol{N}_q d\Gamma_2 \tag{12}$$

where $\boldsymbol{P}(t)$ is the vector of nodal hydrodynamic pressure; $\ddot{\boldsymbol{q}}_a(t)$ is the vector of nodal absolute accelerations of the structure; $\boldsymbol{N}_p(x)$ is the matrix of shape functions corresponding to the hydrodynamic pressure (i.e. $p(x,t)=\boldsymbol{N}_p(x)P(t)$); $\boldsymbol{N}_q(x)$ is the matrix of shape functions corresponding to the displacement of the structure (i.e. $\boldsymbol{q}(x,t)=\boldsymbol{N}_q(x)\boldsymbol{q}(t)$). Moreover, the discrete non-linear equations of motion of the tank subjected to seismic motion and fluid interaction forces, can be written as:

$$\boldsymbol{M}\ddot{\boldsymbol{q}}(t)+\boldsymbol{C}\dot{\boldsymbol{q}}(t)+\boldsymbol{K}\boldsymbol{q}+\boldsymbol{L}_f^T\boldsymbol{F}_u(t)=-\boldsymbol{M}\boldsymbol{R}\ddot{\boldsymbol{d}}_g(t)+\boldsymbol{S}^T\boldsymbol{P}(t) \tag{13}$$

where $\boldsymbol{q}(t)$ is the vector of degrees of freedom (DOFs) of the structure; $\boldsymbol{M},\boldsymbol{K}$, and $\boldsymbol{C}$ are the matrix of mass, stiffness, and viscous damping of the structure, respectively; $\boldsymbol{F}_u(t)$ is the vector of non-linear vertical forces of the devices; $\boldsymbol{L}_f$ is a kinematic transformation matrix; $\ddot{\boldsymbol{d}}_g(t)$ is the vector of ground acceleration, and $\boldsymbol{R}$ is the incidence matrix. Thus, Eqs. (9) and (13) can be written as the following system of coupled equations [28,29]:

$$\begin{bmatrix}\boldsymbol{M}_p & \rho\boldsymbol{S}\\ \boldsymbol{0} & \rho\boldsymbol{M}\end{bmatrix}\begin{bmatrix}\ddot{\boldsymbol{P}}(t)\\ \ddot{\boldsymbol{q}}(t)\end{bmatrix}+\begin{bmatrix}\boldsymbol{0} & \boldsymbol{0}\\ \boldsymbol{0} & \rho\boldsymbol{C}\end{bmatrix}\begin{bmatrix}\dot{\boldsymbol{P}}(t)\\ \dot{\boldsymbol{q}}(t)\end{bmatrix}+\begin{bmatrix}\boldsymbol{K}_p & \boldsymbol{0}\\ -\rho\boldsymbol{S}^T & \rho\boldsymbol{K}\end{bmatrix}\begin{bmatrix}\boldsymbol{P}(t)\\ r\boldsymbol{q}(t)\end{bmatrix}+\begin{bmatrix}\boldsymbol{0}\\ \rho\boldsymbol{L}_f^T\end{bmatrix}\boldsymbol{F}_u(t)=-\begin{bmatrix}\rho\boldsymbol{S}\boldsymbol{R}\\ \rho\boldsymbol{M}\boldsymbol{R}\end{bmatrix}\ddot{\boldsymbol{d}}_g(t) \tag{14}$$

4.1. Quasi-static approach

The propagation velocity of the compression waves in wine is almost the same as in water, i.e. close to 1600 m/s. The natural frequencies of vibration of the wine contained inside the tank are much greater than those of the structure. In addition, the frequency content of earthquakes is generally below 10 Hz, whereby only the low frequency modes of the structure are excited. As a consequence, the fluid perceives the acceleration of the structure $\ddot{\boldsymbol{q}}_a(t)$ as a quasi-static excitation. Thus, Eq. (9) can be approximated as:

$$\boldsymbol{K}_p\boldsymbol{P}(t)\approx-\rho\boldsymbol{S}\ddot{\boldsymbol{q}}_a(t)=-\rho\boldsymbol{S}\left(\ddot{\boldsymbol{q}}(t)+\boldsymbol{R}\ddot{\boldsymbol{d}}_g(t)\right) \tag{15}$$

Because relative pressure on the free surface is assumed equal to zero, the matrix $\boldsymbol{K}_p$ is invertible. Thus, substituting $\boldsymbol{P}(t)$ in Eq. (13), the following equation is obtained:

$$(\boldsymbol{M}+\boldsymbol{M}_f)\ddot{\boldsymbol{q}}(t)+\boldsymbol{C}\dot{\boldsymbol{q}}(t)+\boldsymbol{K}\boldsymbol{q}(t)+\boldsymbol{L}_f^T\boldsymbol{F}_u(t)=-(\boldsymbol{M}+\boldsymbol{M}_f)\boldsymbol{R}\ddot{\boldsymbol{d}}_g(t) \tag{16}$$

where $\boldsymbol{M}_f=\rho\boldsymbol{S}^T\boldsymbol{K}_p^{-1}\boldsymbol{S}$ is the attached fluid mass matrix.

To validate this approach, the model M1, shown in Fig. 10(a) and described in Section 5, was used. The structure was considered fixed to the ground by pinned connection. A constant modal damping $\xi=0.005$ for the fluid and $\xi=0.05$ for the structure was considered. The natural periods of the fluid (i.e. eigenvalues of $\boldsymbol{K}_p$ and $\boldsymbol{M}_p$), and the structure with and without fluid are shown in Fig. 9 (a). There is a difference of two orders of magnitude between the fundamental periods of the fluid and those of the full structure. The model M1 was subjected to the three components of the Curicó seismic record [30]. A comparison of the responses obtained with the Eq. (14) and (16) is presented in Fig. 9(b) and (c). The displacement of the neck of the structure is shown in part (b), while the hydrodynamic pressure on the center of gravity of the fluid is shown in part (c). In both cases, the differences are negligible. Therefore, the results of the dynamic analyses presented in this study correspond to the quasi-static approximation.

5. Case studies

Although the proposed isolation system can be applied to any structure or equipment [24], their use is particularly attractive in legged wine storage tanks. The performance of this type of structures during strong seismic events has not been satisfactory. As noted, the legs of the tanks are one of the critical elements of the structural system, in particular against axial load increments. Loss of wine has been observed due to the increase of pressure of the contained fluid. This increase can be generated by horizontal or vertical accelerations. With the VRI system, it is possible to reduce horizontal and vertical seismic loads, and thus control both the increase of axial load on the legs and the increase of pressure in the fluid.

Two tanks of 304-L stainless steel were analyzed. The first was a tank of 3,000 l with four legs (model M1), while the second was a tank of 30,000 l with six legs (model M2). The geometric properties of the tanks are presented in Table 4. Schemes of model M1 and model M2, which were fully developed in the Matlab environment [31], are shown in Fig. 10. The following simplifications were considered: (i) the bottom of the tank was assumed horizontal; and (ii) special components such as valves and the front manhole (Fig. 1 (a)) were ignored. Four-node shell elements with 6 DOFs per node were used to represent the cylindrical mantle, bottom plate, roof, and neck. The beams of the bottom stiffening system and legs were modeled with frame elements. The fluid was modeled through 8-node isoparametric elements.

Two support conditions were considered: (i) fixed base (FB) by pinned condition; and (ii) legs supported on ISO3D devices, i.e. vertical rocking isolation (VRI) condition. In all cases, material linear elastic behavior was assumed. Nonlinearity was associated only to the vertical displacement of the devices. The dynamic properties of the four considered cases are presented in Table 5. The devices used for base isolation conditions are described in Section 2.3. The ISO3D-B device was used for model M1, while ISO3D-A device was used for model M2.

5.1. Time history analysis results

In this Subsection, the results of the time-history analyses of the four cases considered for this study are presented. The maximum axial load and shear load produced on the legs of the tanks are compared under FB and VRI support conditions.

Eight records of the Maule Earthquake [30] applying the three components of the ground motion were considered. The pseudo-acceleration spectra of the 3 components of these records, for a damping ratio $\xi=0.05$, are shown in Fig. 11.

The non-linear Newmark method was implemented for numerical integration. Newton Raphson iterations were used to achieve convergence at each step. The results of model M1 subjected to the Curicó record are shown in Fig. 12. The time-history response

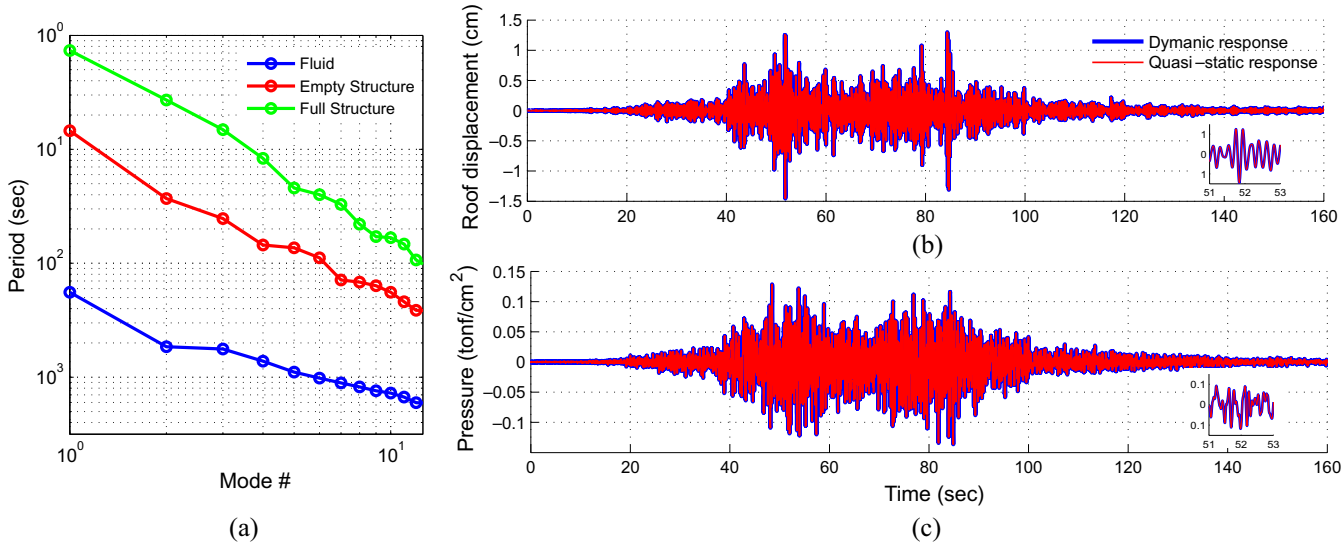

Fig. 9. Cuasi-static response: (a) comparison of periods; (b) roof lateral displacement; (c) hydrodynamic pressure in the center of the tank.

Table 4
Tanks geometric parameters.

Model	Capacity (l)	# legs	Legs height (cm)	Tank radius (cm)	Wall height (cm)
M1	3.000	4	90	75	210
M2	30.000	6	120	160	375

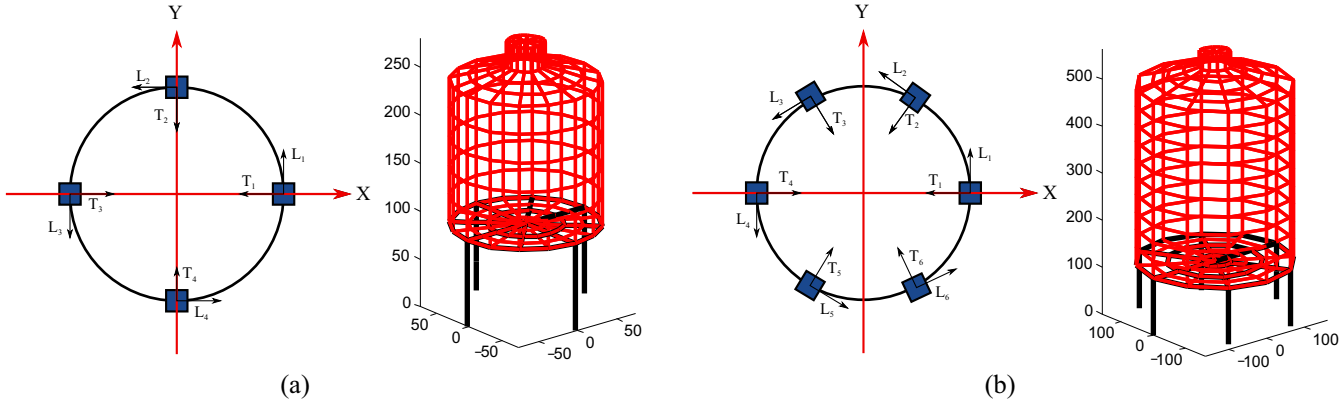

Fig. 10. Tank models considered: (a) Model M1; (b) Model M2.

Table 5
Model M1 and model M2 modal information.

Model	Condition	Mode	Period (sec)	Participating mass ratio X (%)	Participating mass ratio Y (%)	Participating mass ratio Z (%)
M1	FB	1	0.27	100	0	0
		2	0.27	0	100	0
		28	0.04	0	0	37
	VRI	1	1.1	0	89	0
		2	1.1	89	0	0
		3	0.3	0	0	100
M2	FB	1	0.32	73	24	0
		2	0.32	24	73	0
		25	0.08	0	0	57
	VRI	1	1.2	21	62	0
		2	1.2	62	21	0
		3	0.4	0	0	100

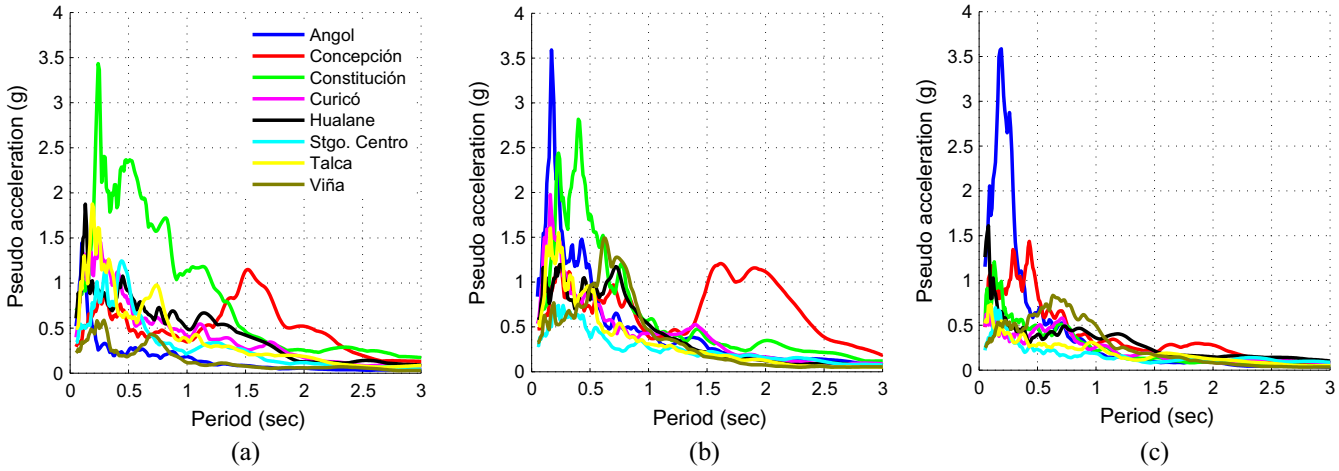

Fig. 11. Response spectra of recorded ground motions for $\xi = 0.05$: (a) transversal direction; (b) longitudinal direction; (c) vertical direction.

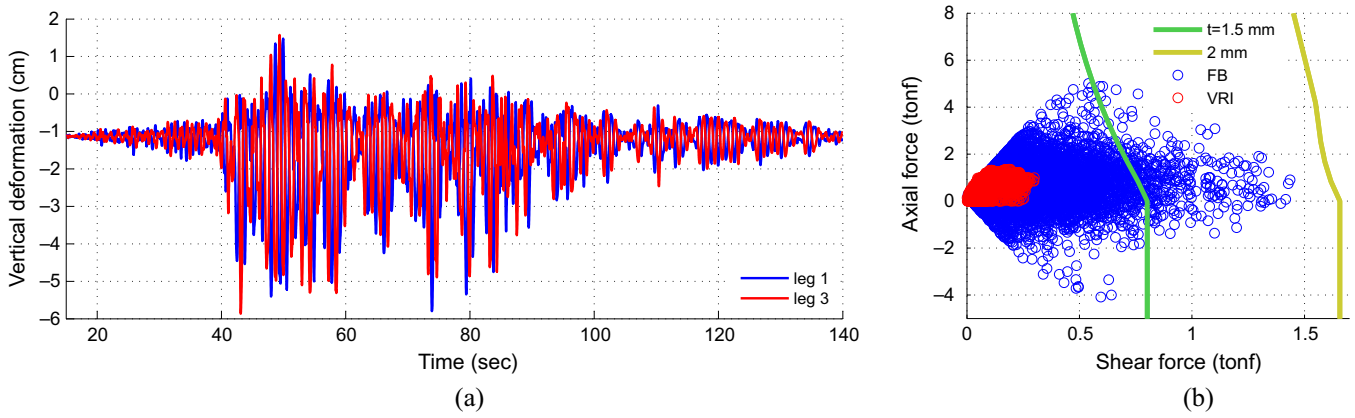

Fig. 12. Time-history response of the model M1 (VRI condition) subjected to Curicó record: (a) Vertical deformation of devices 1 and 3; (b) axial and shear force combinations of device 1.

of the vertical deformation of the devices 1 and 3 for the VRI condition is shown in part (a). Uplift was observed in the devices. However, this does not cause problems, as the analyses have considered the impact forces. Nevertheless, because of the low stiffness of the devices in large deformations, the axial compressive forces obtained are low. The combinations of axial load $N(t)$ and total shear $V(t)$ are shown in part (b). The total shear is defined as:

$$V(t) = \sqrt{V_r^2(t) + V_t^2(t)} \tag{17}$$

where V_r and V_t are the shear load in the radial and tangential directions, respectively. In this case, the results obtained for FB and VRI are represented. As a reference, the ultimate resistance curves (URC) proposed by Ashraf et al. [32] (see Appendix B) for wall thickness $t = 1.5$ mm (used in model M1) and $t = 2$ mm, are shown in this figure. For the FB condition, model M1, a thickness of approximately $t = 2$ mm is needed to avoid failure by local buckling of the legs. This explains why many tanks failed by local buckling during the Maule Earthquake (Fig. 1). The use of ISO3D-B isolators significantly reduce both the axial load and the shear load, ensuring elastic behavior of the legs.

The response of model M2 subjected to Curicó record is shown in Fig. 13. For the FB condition, model M2, a wall thickness of $t = 5$ mm is needed to prevent local buckling failure ($t = 3$ mm was used in model M2). For the VRI condition, a wall thickness of $t = 3$ mm is sufficient to avoid this failure.

Reduction percentages of axial load and shear load on the legs are presented in Table 6. Average reductions of 57% and 61% were obtained for axial loads and shear loads, respectively.

6. Fragility analysis

One of the most widely used tools of performance based engineering are fragility curves, obtained from the Fragility Analysis. These curves show the probability of overcoming a limit state (LS) as a function of earthquake intensity. An Incremental Dynamic Analysis (IDA) [33,34] was used in this study. This approach involves performing a non-linear time-history analysis for a set of seismic records, scaled to increasing intensity levels, determining the performance of the structure for each record and intensity level. With this information it is possible to construct a cumulative probability function, calculating the number of times the limit state was exceeded.

There is currently no clear consensus on how should seismic records be selected, or how they should be scaled [30]. In order to obtain robust results, and considering the recommendations of the Pacific Earthquake Engineering Research Center (PEER), a large number of records have been used.

In this research 20 natural seismic records were used. The records come from four events that occurred in Chile: the Maule Earthquake [30], the Tocopilla Earthquake [35], the Tarapaca

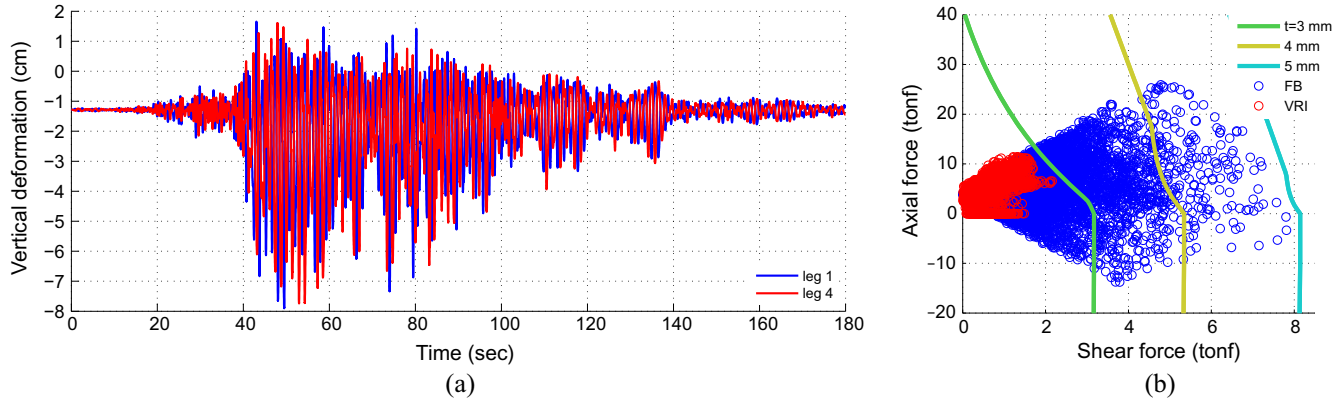

Fig. 13. Time-history response of the model M2 (VRI condition) subjected to Curicó record: (a) vertical deformation of devices 1 and 4; (b) axial and shear force combinations of device 1.

Table 6
Compression and shear loads reduction on legs.

Record	Axial load model M1	Axial load model M2	Shear load model M1	Shear load model M2
Angol	0.85	0.65	0.91	0.73
Concepción	0.40	0.46	0.33	0.30
Constitucón	0.34	0.19	0.64	0.51
Curicó	0.74	0.51	0.83	0.72
Hualane	0.64	0.49	0.73	0.42
Santiago Centro	0.65	0.79	0.53	0.53
Talca	0.79	0.65	0.87	0.78
Viña El Salto	0.35	0.51	0.36	0.45
Mean	0.60	0.53	0.65	0.56

Earthquake [36] and the Algarrobo Earthquake [37]. The records used are presented in Table 7. The ground motions chosen correspond to far-field subduction earthquakes. The reason for this selection is the importance of this type of events in the Chilean wine industry, since almost all vineyards were affected by this type of seismic movements.

The horizontal peak ground acceleration (PGA_h) was used as a measure of intensity, which is defined as:

$$PGA_h = \max\left(\sqrt{\ddot{d}_{gx}^2(t) + \ddot{d}_{gy}^2(t)}\right). \quad (18)$$

Table 7
Seismic records set.

Station	Event	Mw	PGA_h (g)
Viña el Salto	Maule earthquake	8.8	0.45
Santiago Maipú	Maule earthquake	8.8	0.51
Hualañe	Maule earthquake	8.8	0.53
Constitución	Maule earthquake	8.8	0.72
Matanza	Maule earthquake	8.8	0.36
Papudo	Maule earthquake	8.8	0.48
Llolleo	Maule earthquake	8.8	0.58
Curicó	Maule earthquake	8.8	0.50
Talca el Salto	Maule earthquake	8.8	0.51
Angol el Salto	Maule earthquake	8.8	0.70
Concepción	Maule earthquake	8.8	0.40
Mejillones	Tocopilla earthquake	7.8	0.43
Tocopilla SQM	Tocopilla earthquake	7.8	0.67
Tocopilla puerto	Tocopilla earthquake	7.8	0.38
Cuya	Tarapacá earthquake	7.7	0.45
Pica	Tarapacá earthquake	7.7	0.73
Poconchile	Tarapacá earthquake	7.7	0.48
Llay-Llay	Algarrobo earthquake	7.7	0.52
Llolleo	Algarrobo earthquake	7.8	0.74
San Isidro	Algarrobo earthquake	7.8	0.81

where $\ddot{d}_{gx}(t)$ and $\ddot{d}_{gy}(t)$ are the components of the horizontal acceleration. Fifteen levels of PGA_h, equally distributed between 0.2 g and 1.2 g, were selected.

The main types of damage observed during the Maule Earthquake in legged tanks with stiffening systems were: (1) local buckling of legs; (2) pulling of the anchor bolts of the anchoring system; (3) buckling of the screws of the height-adjustment system; and (4) failures by implosion due to sudden loss of wine. The third failure mode does not correspond to failure of the tank itself, whereas the fourth failure mode is generally produced by opening of the front manhole. Therefore, in this study only the first two failure modes have been considered.

It is not necessary to define several failure criteria that rigorously quantify the damage level of the structure under seismic excitation. One LS (failure or not failure) was considered to be sufficient, as the objective of the present work is to compare the performances of the tanks with and without VRI. Failure occurs when any of the two following conditions is reached: (1) there is a combination of axial load and bending moment that initiates the failure by buckling one of the tank's legs (see Appendix B); and (2) the maximum tensile force in any of the legs of the tank exceeds the tensile strength of the anchor. Fragility curves for the four cases studied were obtained by fitting a log-normal function of cumulative probability with a confidence interval of 95%.

The fragility curves obtained for model M1 are shown in Fig. 14 (a). Note that $PGA_h = 0.37$ g and 1.05 g are required to achieve 50% of probability of failure in the FB and VRI condition, respectively. The fragility curves obtained for model M2 are shown in Fig. 14 (b). In this case $PGA_h = 0.36$ g and 0.80 g are required to reach 50% of probability of failure in the FB and VRI condition, respectively.

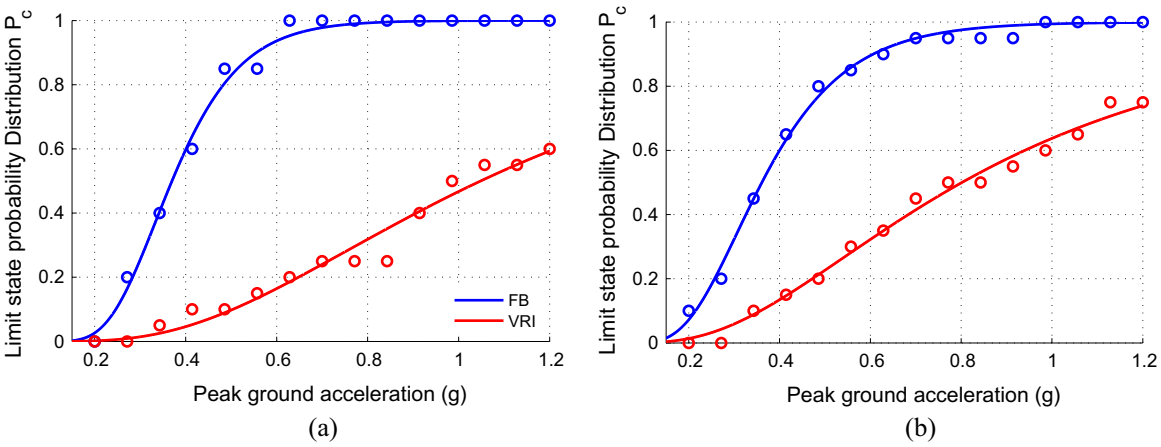

Fig. 14. Seismic fragility relations for the structure with and without seismic isolation: (a) Model M1; (b) Model M2.

7. Conclusions

This research presents a new device called ISO3D, designed for three-dimensional seismic isolation of structures and equipment. The generic constitutive relation of the isolator in the vertical direction was calculated. The equations presented were validated using finite element models and prototype tests. Although the proposed system can be used to protect any structure or equipment, this study focused only on its application to legged wine storage tanks. To evaluate improvements in structural seismic performance, non-linear time-history analyses were conducted and fragility curves were obtained.

The ISO3D device consists of three parts: (1) an articulated frame; (2) a system of springs; and (3) an energy dissipation system. The frame consists of a set of six articulated plates, which form a hexagonal prism. The springs can be classified as primary or secondary. Primary springs provide the flexibility to isolate vibrations, while secondary springs are responsible for preventing excessive vertical deformation caused by the structure's own weight. Deformation would otherwise make vertical seismic isolation through passive devices unfeasible. The energy dissipation system may be comprised by one or more devices, which can deform axially or rotationally. The device is flexible in the vertical and transversal axes, but is stiff in the longitudinal axis; therefore, the device must be placed in such a way that the supported structure has three flexible modes of vibration: one vertical mode, and two rocking modes.

While there are several possible materializations for the device, results are presented for two types of devices, called ISO3D-A and ISO3D-B. The first is formed by at least one compression spring in the vertical direction, and at least two tension springs in the horizontal direction. The second device is formed by at least two torsion springs located on the axis connecting the inclined plates of the device. For both types, simplified expressions are proposed to represent vertical force-deformation relation. These expressions show very similar results compared to finite element models. Prototype tests were performed, with results close to numerical predictions. However, for practical applications better joints must be made to minimize existing friction, especially in the ISO3D-B prototype.

Although the proposed system can be applied to any type of structure, it is particularly attractive as a seismic protection system for special structures, such as legged fluid storage tanks, power transformers, and sensitive equipment with vertical acceleration. In this study, an application for legged wine storage tanks is presented. These structures were severely damaged during the Maule Earthquake, mainly by local buckling of the legs. Two models were studied: a tank with 3 m^3 of capacity with 4 legs (model M1), and a tank with 30 m^3 of capacity with 6 legs (model M2). A quasi-static approach was used to consider the fluid-structure interaction, where the fluid behaves as a mass attached to the tank walls. For each model, two support conditions were considered: (i) fixed-base (FB); and (ii) vertical-rocking isolation (VRI) support.

Three-dimensional time-history analyses of fixed base tanks show excessive stress demand on the legs, which explains why many of such structures failed (and even collapsed) during the Maule Earthquake. By using the VRI system, reductions of 67% of shear load and of 45% of axial load were obtained for model M1, and of 57% and 61% respectively, for model M2. Note that these values are comparable to those typically obtained by conventional lateral isolation systems.

Finally, a Fragility Analysis was performed using 20 natural records corresponding to four large earthquakes in Chile. The analysis shows that the PGA that is responsible for 50% of the probability of failure in model M1 increases by an average of 184% when using VRI. For model M2, there was an increase of 122%.

Acknowledgements

This research has been funded by Comisión Nacional de Investigación Científica y Tecnológica CONICYT (through the FONDECYT Project No. 1120937, FONDEQUIP Project EQM120198, and CONICYT-PCHA/MagisterNacional/2015-22151113), and Pontificia Universidad Católica de Chile throught the I Competition Accelerator Program UC. The authors are grateful for this support.

Appendix A. Prototype test

Two small prototypes, one for each type, were built. These prototypes were subjected to cyclic tests with quasi-static controlled vertical displacement. The measured force-deformation relation is presented in Fig. A.15. As expected, the relation has hysteretic behavior due to friction in the connections. This effect is more significant in the ISO3D-B device, because such connections do not have any special treatment to minimize friction. For the ISO3D-A device, the effect is less significant because the connections are built with high quality commercial hinges. However, considering only the contribution of the springs (i.e. ignoring the hysteretic part) numerical predictions and experimental results were similar. The main properties of the prototypes are presented in Table A.8.

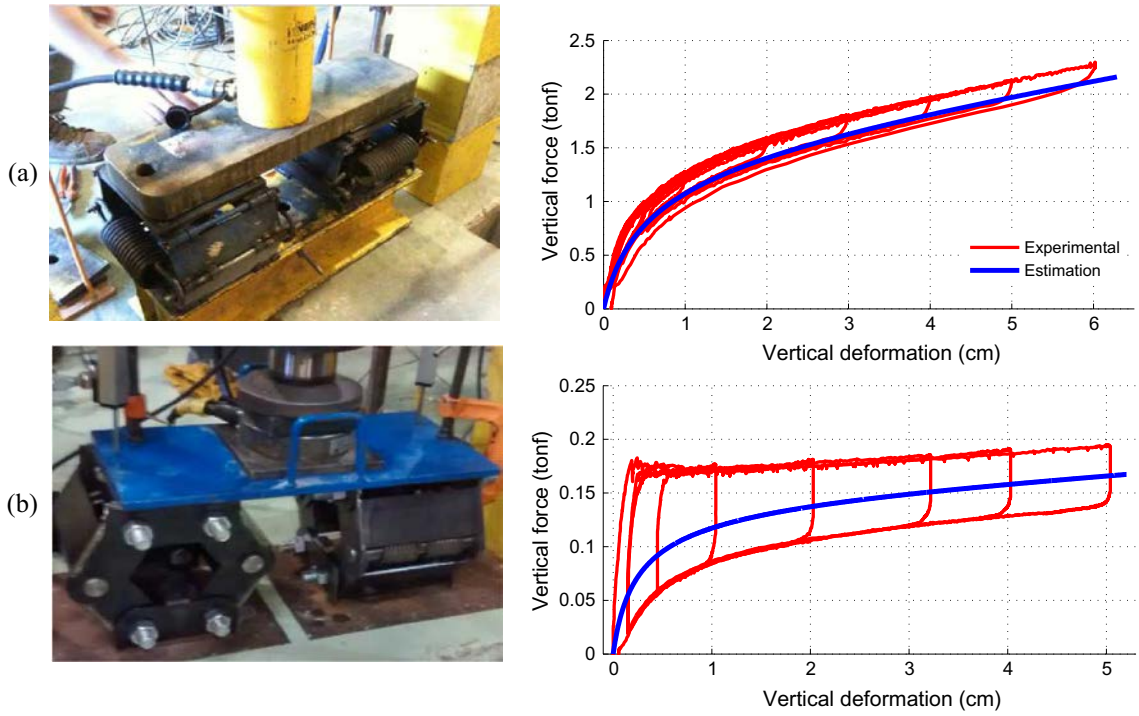

Fig. A.15. Experimental results: (a) ISO3D-A prototype; (b) ISO3D-B prototype.

Table A.8
Tested prototypes properties.

Device	L (cm)	b_0 (cm)	spring type	# springs	d (cm)	D (cm)	N_a
ISO3D-A	8	1.5	compression	1	1.2	6.0	4.5
			compression	1	0.8	5.2	8
			tension	2	0.9	5.4	13
ISO3D-B	8.5	1.0	torsional	4	0.5	3	8

Appendix B. Elastic legs buckling resistance

As has been demonstrated by Ashraf et al. [32], Gardner and Ashraf [38] and Ashraf et al. [39], the behavior of the legs of the tank is controlled by the local buckling of one of the components of its cross-section. The equation proposed to treat the axial-bending interaction in structural stainless steel members has the following form:

$$G(N, M_y, M_z) = \frac{N}{(N_{RD})_{min}} + \frac{\kappa_y M_y}{a_{g,y} W_{el,y} \sigma_{0.2}} + \frac{\kappa_z M_z}{a_{g,z} W_{el,z} \sigma_{0.2}} \leqslant 1 \qquad \text{(B.1)}$$

where N is the axial load; M_y and M_z are the bending moments acting in the Y-axis and the Z-axis of the section; $(N_{RD})_{min}$ is the minimum compression resistance of cross-section; κ_j is the beam-column interaction factor; $a_{g,j}$ is the generalized shape factor of cross-section; $W_{el,j}$ is the elastic modulus; and the subscripts $j = y, z$ refer to the Y-direction and Z-direction respectively.

References

[1] Shrimali M, Jangid R. Seismic analysis of base-isolated liquid storage tanks. J Sound Vib 2004;275(1):59–75.
[2] Cho KH, Kim MK, Lim YM, Cho SY. Seismic response of base isolated liquid storage tanks considering fluid-structure-soil interaction in time domain. Soil Dyn Earthquake Eng 2004;24(11):839–52.
[3] Panchal V, Jangid R. Variable friction pendulum system for seismic isolation of liquid storage tanks. Nucl Eng Des 2008;238(6):1304–15.
[4] Panchal V, Jangid R. Behaviour of liquid storage tanks with VCFPS under near-fault ground motions. Struct Infrastruct Eng 2012;8(1):71–88.
[5] Abal E, Uckan E. Parametric analysis of liquid storage tanks base isolated by curved surface sliding bearings. Soil Dyn Earthquake Eng 2010;30(1):21–31.
[6] Shekari M, Khaji N, Ahmadi M. On the seismic behavior of cylindrical base-isolated liquid storage tanks excited by long-period ground motions. Soil Dyn Earthquake Eng 2010;30(10):968–80.
[7] Soni D, Mistry B, Panchal V. Double variable frequency pendulum isolator for seismic isolation of liquid storage tanks. Nucl Eng Des 2010;241(3):700–13.
[8] Foti D, Catalan A, Vacca S. On the dynamic response of rolling base isolation systems. Struct Control Health Monit 2013;20(4):;639–48.
[9] Menga N, Foti D, Carbone G. Evaluation and improvement of the design of RLRB rolling devices for seismic isolation. Meccanica 2017:1–11. https://doi.org/10.1007/s11012-016-0612-y. ISSN: 0025-6455.
[10] Foti D, Diaferio M, Nobile R. Dynamic behavior of new aluminum-steel energy dissipating devices. Struct Control Health Monit 2017;20(7):1106–19.
[11] Silvestri S, Gasparini G, Trombetti T, Foti D. On the evaluation of the horizontal forces produced by grain-like inside silos during earthquakes. Bull Earthq Eng 2012;10:1535–60.
[12] Silvestri S, Ivorra S, Di Chiacchio L, Trombetti T, Foti D, Gasparini G, et al. Shaking-table tests of flat-bottom circular silos containing grain-like material. Earthquake Eng Struct Dyn 2016;45(1):69–89.
[13] Cooper D. A history of steel tank structural design. Wine Bus Monthly 2004.
[14] IDIA. El sismo de Caucete, San Juan, Argentina, del 23 de noviembre de 1977 y la seguridad que proveen las normas sismoresistentes. Seminario internacional de preparación para atención de catástrofes, Viña del Mar, Chile, Marzo 1978; 1987 [in Spanish].
[15] Manos G. Evaluation of the earthquake performance of anchored wine tanks during the San Juan, Argentina, 1977 Earthquake. Earthquake Eng Struct Dyn 1991;20:1099–114.
[16] Niwa A, Clough R. Buckling of cylindrical liquid-storage tanks under earthquake loading. Earthquake Eng Struct Dyn 2004;10(1):107–22.
[17] Swan W, Miller D, Yanev P. The Morgan Hill Earthquake of april 24, 1984-effects on industrial facilities, buildings, and other facilities. Earthquake Spectra 1985;1(3):457–568.
[18] EERI Reconnaissance Team. Loma Prieta, California, Earthquake of October 15, 1989: reconnaissance report. Earthquake Spectra 1990;6(S1):1–448.

[19] EERI Reconnaissance Team. Preliminary report on the 22 December 2003, M 6.5 San Simeon, California Earthquake. Seismological Research Letters 2004;75 (2):155–72.
[20] Lomax W, Walker A, Wood R. Implementing a holistic ductile design approach to stainless steel wine storage tanks. In: 16th world conference on earthquake engineering 2017; 16WCEE 2017.
[21] Sandoval V. Análisis de los efectos del terremoto del 27 de febrero de 2010 en estanques de acero inoxidable de pared delgada (EAIPD) con patas y desarrollo de un sistema de protección sísmica para estas estructuras [MSc thesis]. Pontificia Universidad Catlica de Chile; 2011 [in Spanish].
[22] González E, Almazán JL, Beltrán J, Herrera R, Sandoval V. Performance of stainless steel winery tanks during the 02/27/2010 Maule Earthquake. Eng Struct 2013;56:1402–18.
[23] Almazán JL, Cerda FA, De la Llera JC, López-García D. Linear isolation of stainless steel legged thin-walled tanks. Eng Struct 2007;29(7):1596–611.
[24] Almazán JL. A new nonlinear system for three-dimensional isolation of vibration in structures and equipment. In: 10th US national conference on earthquake engineering. Anchorage, Alaska; 2014.
[25] González A. Estudio teórico-experimemtal de aislamiento sísmico en estanques de acero inoxidable de pared delgada (EAIPD) con apoyos [MSc thesis]. Pontificia Universidad Catlica de Chile; 2009 [in Spanish].
[26] Shigley EJ, Mischke RC, Brown HT. Standard handbook of machine design. PTR Prentice Hall Inform Syst Sci Ser 2004:198.
[27] Lee HH. Finite element simulations with ANSYS Workbench 14. SDC Publications; 2012.
[28] Zeinkiewicz O, Taylor R, Zhu J. The finite element method: its basis and fundamentals. Elsevier Butterworth-Heinemann; 2005.
[29] Auad G. Aislamiento sísmico no lineal vertical-rotacional: Aplicación a estanques de apoyo discontinuo [MSc thesis]. Pontificia Universidad Catlica de Chile; 2015 [in Spanish].
[30] Boroschek R, Soto P, Leon R. Registros del terremoto del maule Mw= 8.8 27 de febrero de 2010. Red Nacional de Acelerógrafos del Departamento de Ingeniería Civil, Facultad de Ciencias Físicas y Matemáticas, Universidad de Chile, Informe RENADIC, 10(05); 2010. p. 100 [in Spanish].
[31] Hunt BR, Lipsman RL, Rosenberg JM. A guide to MATLAB: for beginners and experienced users. Cambridge University Press; 2014.
[32] Ashraf M, Gardner L, Nethercot D. Structural stainless steel design: resistance based on deformation capacity. Struct Eng 2008;134:402–11.
[33] Vamvatsikos D, Cornell CA. Incremental dynamic analysis. Earthquake Eng Struct Dyn 2002;31:491–514.
[34] Vamvatsikos D, Fragiadakis M. Incremental dynamic analysis for estimating seismic performance sensitivity and uncertainty. Earthquake Eng Struct Dyn 2009;39:141–63.
[35] Boroschek R, Soto P, Leon R. Terremoto del norte de chile 14 de noviembre de 2007 m=7.7 informe preliminar #4. Red Nacional de Acelerógrafos del Departamento de Ingeniería Civil, Facultad de Ciencias Físicas y Matemáticas, Universidad de Chile, Informe RENADIC; 2007 [in Spanish].
[36] Boroschek R, Soto P, Leon R. Terremoto de tarapacá 13 de junio de 2005. Red Nacional de Acelerógrafos del Departamento de Ingeniería Civil, Facultad de Ciencias Físicas y Matemáticas, Universidad de Chile, Informe RENADIC; 2005 [in Spanish].
[37] Gobierno de Chile. Oficina Nacional de Emergencia ONEMI 2009. Consolidado sismo destructivo del 3 de marzo de 1985 [in Spanish].
[38] Gardner L, Ashraf M. Structural design for non-linear metallic materials. Eng Struct 2006;28:926–34.
[39] Ashraf M, Gardner L, Nethercot DA. Compression strength of stainless steel cross-sections. Eng Struct 2006;28:926–34.